ChemCatChem

Research Article
doi.org/10.1002/cctc.202200149

Chemistry Europe
European Chemical Societies Publishing

www.chemcatchem.org

Supported $Ru_xIr_{1-x}O_2$ Mixed Oxides Catalysts for Propane Combustion: Resistance Against Water Poisoning

Zheng Wang,[a, b] Wei Wang,[a, b] Omeir Khalid,[b] Tim Weber,[b] Alexander Spriewald Luciano,[b] Wangcheng Zhan,*[a] Bernd M. Smarsly,*[b] and Herbert Over*[b]

Mixed oxide catalysts $Ru_xIr_{1-x}O_2$ with varying composition x (x = 0, 0.25, 0.5, 0.75, 1.0) supported on CeO_2, γ-Al_2O_3 or ZrO_2 are successfully prepared and tested in the catalytic propane combustion in terms of activity and stability. Pure IrO_2 reveals a significantly lower activity than $Ru_xIr_{1-x}O_2$ with $x \geq 0.25$. For low conversion, pure RuO_2 on CeO_2 turns out to be the most active catalyst, while at higher conversion, $Ru_{0.75}Ir_{0.25}O_2$ on ZrO_2 is found to be more active than RuO_2, pointing towards synergism of Ru and Ir sites. Long-term stability and also the resistance against water poisoning are highest for ZrO_2-supported catalysts. The higher the Ir concentration in the active component $Ru_xIr_{1-x}O_2$ the more susceptible is the catalyst to water poisoning. Water poisoning is shown to be reversible, consistent with a blocking of catalytically active sites by water adsorption.

Introduction

Short chain alkanes are used as fuels for the propulsion of engines,[1] because they combust relatively cleanly with respect to soot formation and sulfur dioxide emission and also due to the higher atomic hydrogen-to-carbon ratio associated with a lower carbon footprint per unit energy, compared e.g. to gasoline. For instance, methane reveals the highest hydrogen-to-carbon ratio of 4:1, while propane with H:C = 8:3 is easy to liquefy, thus increasing the energy density considerably in comparison to methane. This aspect is particularly relevant, as liquid petroleum gas (LPG) is used to fuel internal combustion engines and thereby constitutes the third most widely used engine fuel world-wide. Besides using as energy carrier, LPG is a feedstock in the chemical industry for the synthesis of other olefins. However, the release of residual propane from the exhaust gases of LPG-fueled engines and the operation of refineries to the atmosphere is of environmental concern due to photochemical reactions with NO_x and other air-borne chemicals, causing photochemical smog. Hence it is necessary to prevent slip of propane and other short-chain alkanes to the atmosphere by complete catalytic combustion.

For the catalytic combustion of methane, Pd-based materials are considered as the most active catalysts, while Pt-based catalysts are preferred for the combustion of higher alkanes.[2–6] During the past years, noble metal-based materials (such as Pt, Pd, Rh, Au)[2,7–15] and non-noble metal oxides (such as Co, Mn, Ni)[16–20] have been synthesized and applied as catalyst to the propane combustion reaction. Ruthenium is known to be one of the most active elements in the activation of C–H and C–C bonds,[21] thus making it a promising and less expensive alternative to Pt for the removal of higher hydrocarbons. In several studies the excellent activity of Ru-based catalysts in propane combustion has been demonstrated.[22–27] For example, for the same feed gas and gas hourly space velocity, the activity of Ru/CeO_2 sample is 1.5 times higher than that that of Pt/ZSM–S catalysts at 200 °C.[25,28] However, Ru-based catalysts tend to deactivate via loss of active surface area by sintering or by transformation into volatile RuO_4 at higher temperatures. Therefore, several studies pursued the preparation of solid solutions to stabilize Ru-based catalysts in propane combustion. For example, Ledwa et al.[29–30] used $Ru_xCe_{1-x}O_{2-y}$ to stabilize the nanoparticles' morphology, i.e. using a solid solution of metal oxides. As a different concept, Adamska et al.[31] and Baranowska et al.[32–34] modified Ru-Al_2O_3 material with Mo and Re, generating bimetallic Ru alloy nanoparticles. Liu et al.[35] introduced unsaturated pentacoordinate Al^{3+} sites to stabilize a Ru-CeO_x catalyst. Chen et al.[36] prepared a Ru–Ag alloy with improved stability in catalytic oxidation of propane. An alternative and promising approach to stabilize RuO_2 is the solid solution with IrO_2, i.e., $Ru_xIr_{1-x}O_2$, which are intensively studied in water electrolysis.[37–38]

Recently, the solid solutions $Ru_xIr_{1-x}O_2$ with various compositions x have been reported to reveal a synergetic effect in the catalytic methane combustion.[39–40] While IrO_2 is required to activate methane, RuO_2 was shown to be an excellent catalyst for subsequent oxidation steps to form water and CO_2. In these

[a] Z. Wang, W. Wang, Prof. W. Zhan
Research Institute of Industrial Catalysis
School of Chemistry and Molecular Engineering
East China University of Science and Technology
No. 130, Meilong Road
Shanghai 200237 (P.R. China)
E-mail: Zhanwc@ecust.edu.cn

[b] Z. Wang, W. Wang, Dr. O. Khalid, T. Weber, A. Spriewald Luciano, Prof. B. M. Smarsly, Prof. H. Over
Institute of Physical Chemistry
Justus Liebig University
Heinrich-Buff-Ring 17
D-35392, Giessen (Germany)
E-mail: Bernd.Smarsly@phys.Chemie.uni-giessen.de
Herbert.Over@phys.chemie.uni-giessen.de
Homepage: https://www.uni-giessen.de/fbz/fb08/Inst/physchem/over

Supporting information for this article is available on the WWW under https://doi.org/10.1002/cctc.202200149

studies the composition $Ir_{0.125}Ru_{0.875}O_2$ exhibited the best performance, i.e. quite moderate Ir contents were sufficient to endow such catalyst materials with significant potential to activate methane. Hence, here we address the question, if this insight can be transferred also to the catalytic combustion of propane.

In the alkane combustion process, water in the reaction feed or produced by the reaction is known to hamper the catalytic combustion reaction,[41–42] a problem that has already been studied extensively for the methane combustion[4,43–46] but to lesser extent for the catalytic propane combustion, employing Pd and Pt-based catalysts.[47–50] For example, Murata et al.[51] found that hydrophobic carrier (α-Al_2O_3) reduces water poisoning in the methane combustion reaction over supported PdO, while Huang et al.[52] used water sorbent that was physically mixed with Pd/CeO_2 catalyst to enhance the activity of methane combustion. Since water possibly impedes the catalytic combustion by blocking the active sites, one would expect that water poisoning is equally important in the catalytic propane combustion over $Ru_xIr_{1-x}O_2$-based catalysts and this poisoning effect may depend critically on the composition x of $Ru_xIr_{1-x}O_2$ and on the specific carrier material.

In this report we present activity and stability tests for the catalytic propane combustion over 5 mol% $Ru_xIr_{1-x}O_2$ ($x=0$, 0.25, 0.5, 0.75, 1.0) supported on CeO_2, γ-Al_2O_3 or ZrO_2. These supports were chosen, because CeO_2 was reported to spur combustion reactions owing to oxygen vacancies,[30] and on the other hand γ-Al_2O_3 and ZrO_2 are commonly used carriers with particularly high chemical stability. Hence, this selection of carriers is considered to allow for gaining insight into an optimum synergistic effect not only with respect to the composition x of $Ru_xIr_{1-x}O_2$, but also into the interaction with the substrates, targeting high activity as well as stability of the catalyst material.

Characterization of the catalysts

Textural properties of the samples

The XRD patterns of the $Ru_xIr_{1-x}O_2$ catalysts supported on various carriers (CeO_2, γ-Al_2O_3 and ZrO_2) are summarized in Figure 1. LaB_6 is physically mixed into the catalyst in order to provide sharp reflections at $2\theta=30.4°$, 37.4 °, 43.5°, and 48.9° (JCPDS card NO. 34-0427) for a precise calibration of the 2θ axis. The main reflections of the cubic CeO_2 carrier are at $2\theta=$ 28.6°, 33.1°, 47.5°, and 56.3° (JCPDS card NO. 34-0394), those of γ-Al_2O_3 (JCPDS card NO. 10-0425) are observed at $2\theta=31.9°$, 37.6°, 39.5° and 45.9°, while the reflections at $2\theta=28.2°$, 31.5° and 34.2° are ascribed to the monoclinic phase of the ZrO_2 support (JCPDS card NO. 37-1484). For Ruxxx_Ce samples (Figure 1A), a weak $Ru_xIr_{1-x}O_2$ (101) diffraction peak appears that continuously shifts from that of RuO_2 to IrO_2 (see the magnified region of XRD patterns in Figure 1B). This clearly indicates that mixed $Ru_xIr_{1-x}O_2$ is formed on CeO_2.[39] Employing Vegard's law, the composition x of $Ru_xIr_{1-x}O_2$ can be derived from the peak position of $Ru_xIr_{1-x}O_2$(101) as shown in Figure S1 and compiled in Table 1. The compositions of Ru075_Ce and Ru050_Ce samples turn out to be 0.79 and 0.63, respectively, being close to the nominal composition of 0.75 and 0.50 and agree well with element analysis (cf. Table S4). From the full-width-at-half-maximum (FWHM) of the (101) reflections, the crystallite sizes of $Ru_xIr_{1-x}O_2$ can be estimated by Scherrer's equation (cf. Table 2), which range from 30 to 53 nm.

For Ruxxx_Al samples (Figure 1C), strong rutile $Ru_xIr_{1-x}O_2$ reflections ((110), (101), and (200)) are discernible in the XRD patterns. Again the rutile (101) reflection shifts continuously in position from that of RuO_2 towards that of IrO_2 (Figure 1D), while for the rutile (110) and (200) reflections the positions remain constant in accordance with previous studies.[39–40] Since the rutile $Ru_xIr_{1-x}O_2$ (101) reflections are intense, the composition x of mixed $Ru_xIr_{1-x}O_2$ can be derived by Vegard's law with high confidence (cf. Figure S1). The derived values are compiled in Table 1 and are close to the nominal compositions. From the FWHM, the crystallite size of RuO_2 turns out to be 23 nm, while for the other $Ru_xIr_{1-x}O_2$ samples, the crystallite size is in the range of 11–13 nm. Surprisingly, the crystallite size of Ruxxx_Ce

Table 1. XRD analysis of $Ru_xIr_{1-x}O_2$ on different supports: Full-width-at-half-maximum (FWHM) and peak position of (101), composition of $Ru_xIr_{1-x}O_2$ of the supported samples derived by Vegard's law, the crystallite size of $Ru_xIr_{1-x}O_2$ calculated by Scherrer equation, based on the rutile (101) reflection.

$Ru_xIr_{1-x}O_2$ (101)		Ru100	Ru075	Ru050	Ru025	Ir100
CeO_2	FWHM [° 2theta]	0.15	0.19	0.28	–	0.25
	peak position [°]	35.07	35.01	34.96	–	34.70
	x ($Ru_xIr_{1-x}O_2$)	1	0.79	0.63	–	0
	crystallite size [nm]	53	43	30	–	33
γ-Al_2O_3	FWHM [° 2theta]	0.36	0.62	0.73	0.71	0.75
	peak position [°]	35.07	35.00	34.93	34.85	34.77
	x ($Ru_xIr_{1-x}O_2$)	1	0.75	0.51	0.24	0
	crystallite size [nm]	23	13	11	12	11
ZrO_2	FWHM [° 2theta]	0.39	0.65	0.69	0.70	0.62
	peak position [°]	35.07	34.99	34.90	34.82	34.74-
	x ($Ru_xIr_{1-x}O_2$)	100	0.73	0.42	0.16	0
	crystallite size [nm]	21	13	12	12	13

Table 2. XPS-derived compositions of the $Ru_xIr_{1-x}O_2$ supported on various carriers.

Properties		Ru100	Ru075	Ru050	Ru025	Ir100
Ru/(Ru + Ir)	nominal	100	75	50	25	0
[mol%]	XPS-derived (CeO_2)	100	68	46	29	0
	XPS-derived (γ-Al_2O_3)	100	72	48	24	0
	XPS-derived (ZrO_2)	100	75	46	25	0
(Ru + Ir)/	nominal	5	5	5	5	5
(Ru + Ir +	XPS-derived (CeO_2)	11	17	17	19	17
Ce/Zr/Al)	XPS-derived (γ-Al_2O_3)	3	4	5	5	5
[mol%]	XPS-derived (ZrO_2)	7	8	11	16	13
$Ir^0/(Ir^0+Ir^{4+})$	XPS-derived (CeO_2)	–	7	8	10	9
[mol%]	XPS-derived (γ-Al_2O_3)	–	4	8	9	9
	XPS-derived (ZrO_2)	–	10	6	10	9

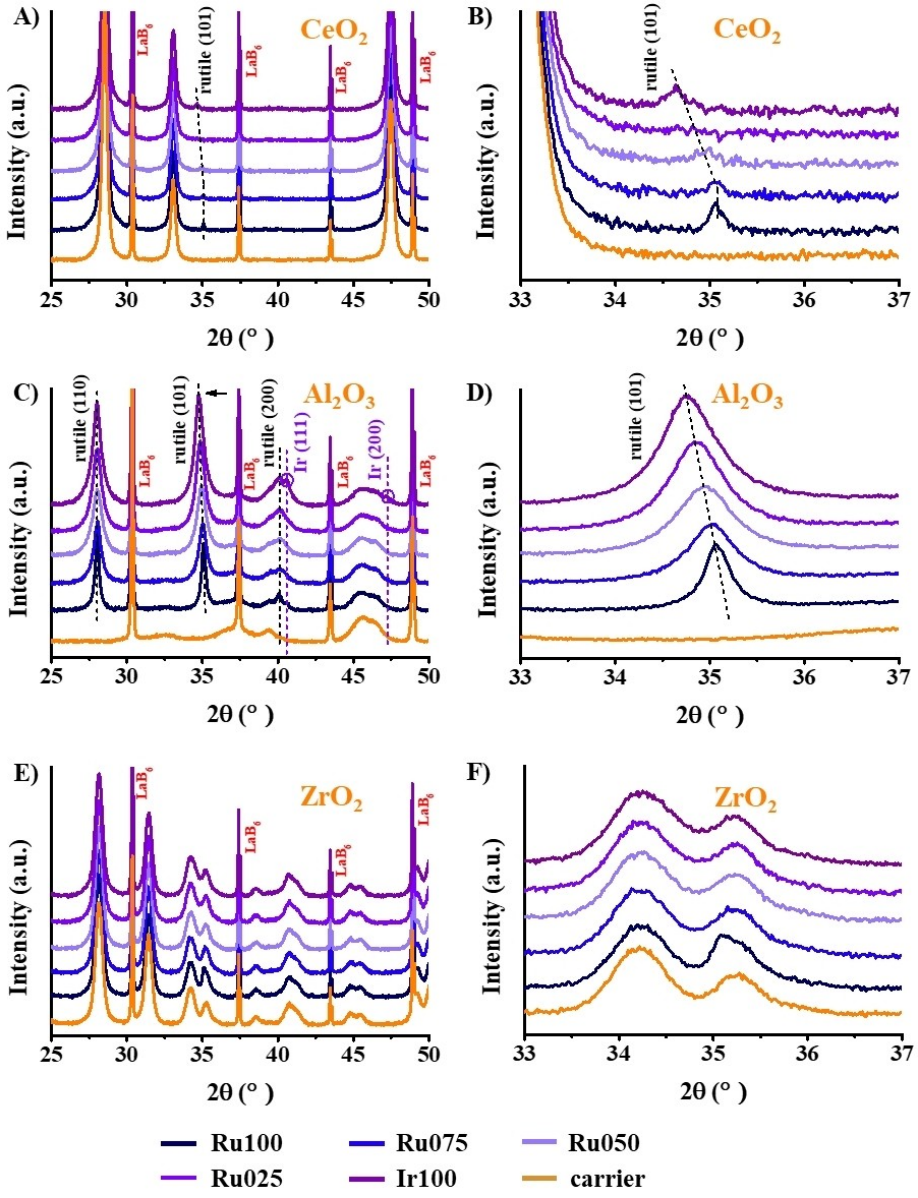

Figure 1. Overview of XRD (A, C, E) and magnified XRD (B, D, F) scans of $Ru_xIr_{1-x}O_2$ supported on CeO_2 (A, B), γ-Al_2O_3 (C, D) and ZrO_2 (E, F) catalysts. The dotted lines in B) and D) may guide the reader to follow the changes in intensity of the minimum at 34.8°.

is significantly larger than those of Ruxxx_Al although the diffraction intensities are substantially smaller. There are two possible effects that may cause the low diffraction intensity of $Ru_xIr_{1-x}O_2$. First, the high atomic number of CeO_2, leads to a comparably stronger absorption of X-rays than for alumina so that the $Ru_xIr_{1-x}O_2$ related diffraction intensity is significantly lower in case of CeO_2 compared to γ-Al_2O_3. Secondly, most of the $Ru_xIr_{1-x}O_2$ particles on CeO_2 are probably X-ray amorphous (crystallite size is below 2 nm). For pure IrO_2 supported on γ-Al_2O_3 (Ir100_Al sample), rutile IrO_2 (110) coexists with the cubic phase of Ir metal ((111), (200)), while for the Ru100_Al sample, only rutile RuO_2 signals are observable in XRD.

Figure 1E summarizes the XRD patterns of the Ruxxx_Zr samples. The diffraction peaks of ZrO_2 overlap with those of rutile ((110), (101)) so that $Ru_xIr_{1-x}O_2$-related features are hardly discernible. For the further analysis the ZrO_2 peaks of the pure carrier at $2\theta = 34.2°$ and 35.3° (cf. Figure 1F) are subtracted from XRD scans of the supported samples (Figure S2), revealing a faint rutile (101) feature whose position varies systematically with the composition *x* according to Vegard's law (cf. Figure S1). From the FWHM of the rutile (101) reflection in Figure S2, the crystallite size of $Ru_xIr_{1-x}O_2$ turns out to be 12–21 nm. Since the diffraction intensities are very small, we conclude that most of the $Ru_xIr_{1-x}O_2$ particles on ZrO_2 are X-ray amorphous.

The Raman spectra of $Ru_xIr_{1-x}O_2$-supported catalysts are summarized in Figure 2 which are similar to those from a previous study of $Ru_xIr_{1-x}O_2$-supported on TiO_2.[40] For all supported samples, two spectral features (the B2g and Eg

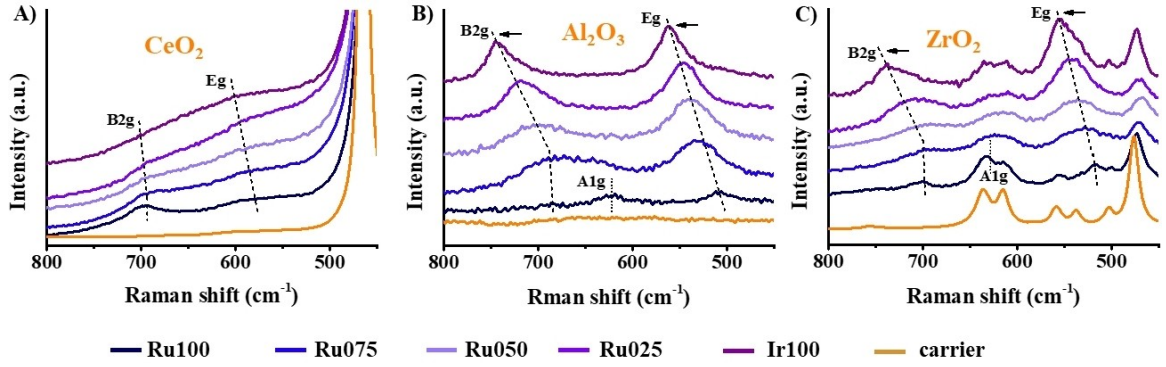

Figure 2. Raman spectra of $Ru_xIr_{1-x}O_2$ supported on CeO_2 (A), γ-Al_2O_3 (B) and ZrO_2 (C).

modes) are assigned to the rutile structure of $Ru_xIr_{1-x}O_2$. The continuous shift of the B2g and Eg peak positions of RuO_2 to those of IrO_2 corroborates the formation of mixed oxide particles. However, for fixed composition *x* of $Ru_xIr_{1-x}O_2$, the wavenumbers of the vibrational features B2g and Eg vary among the carriers, thus indicating a different interaction (due likely to different strain at the interface) between $Ru_xIr_{1-x}O_2$ and the various carriers.

Morphology of the samples

HADDF-STEM micrographs and elemental maps of Ru025_Ce, Ru050_Al and Ru075_Zr are compiled in Figure 3, while corresponding STEM micrographs are shown in Figure S3. These specific compositions of $Ru_xIr_{1-x}O_2$ are chosen since they reveal superior catalytic performance at high conversions for the given carrier material.

Since the lattice d-spacings of $Ru_xIr_{1-x}O_2$ and CeO_2 or ZrO_2 are similar and the contrast of the Ru/Ir species on the CeO_2 and ZrO_2 supports is low, Ru/Ir-containing particles are difficult to discern in STEM images of Ru025_Ce and Ru075_Zr samples. However, element mappings of Ru025_Ce, Ru050_Al and Ru075_Zr presented in Figure 3 clearly reveal that Ru/Ir species are quite homogeneously distributed across the CeO_2 or ZrO_2 carriers. Magnified STEM micrographs and elemental maps for Ru025_Ce and Ru075_Zr in Figure S4 reveal both small (about 2 nm) and larger particles. The latter ones are confirmed by XRD, while the smaller ones are not visible in XRD. For the γ-Al_2O_3 carrier, the contrast is much higher so that Ru/Ir agglomerates (cf. Figure S4) and small particles (cf. Figure S3) in other regions of the sample are visible in STEM.

Composition and dispersion of $Ru_xIr_{1-x}O_2$: XPS analysis

To clarify the surface composition and chemical state of $Ru_xIr_{1-x}O_2$ in the various samples, XPS experiments are conducted. Figure 4 and Figure S5 show the Ru 3d and Ir 4f spectra of the $Ru_xIr_{1-x}O_2$ supported on ZrO_2. All Ru 3d spectra are dominated by C1s. From the energetic position of $Ru3d_{5/2}$ and $Ru3d_{3/2}$ components at around 280.6 eV and 284.8 eV, respectively, we infer that Ru is in the RuO_2 state. This conclusion is further corroborated by the intense satellite feature (black) that is indicative of RuO_2.[53] All Ir 4f spectra show intense Ir^{4+} features and weak Ir^0 features that were also observed in a previous study.[39] The molar ratio of $Ir^0/(Ir^{4+}+Ir^0)$ is in the range of 6–10 mol% (Table 2). Similar values are derived from XPS experiments (Figures S6, S7) for $Ru_xIr_{1-x}O_2$ supported on CeO_2 and γ-Al_2O_3 carriers. The molar ratios of Ru/(Ru + Ir) as determined by XPS are all closed to the nominal values. (cf. Table 2). To quantify the molar ratio of (Ru + Ir)/(Ru + Ir + Ce/Al/Zr) of various $Ru_xIr_{1-x}O_2$ supported samples, we used the Ru 3d, Ir 4f, Ce 3d, Zr 3d and Al 2p XP spectra (cf. Figure S8 and Table 2), because these spectra contain similar depth information. The molar ratio of (Ru + Ir)/(Ru + Ir + Ce/Zr/Al) as summarized in Table 2 are related to the dispersion of the active component. Obviously $Ru_xIr_{1-x}O_2$ on CeO_2 and ZrO_2 reveal significantly higher dispersions than on γ-Al_2O_3, consistent with STEM and XRD experiments (cf. Figures 1, 3).

Catalytic performance of samples in the propane combustion reaction

Figure 5 shows the activity in the form of the space time yield (*STY*) as a function of reaction temperature *T* for propane combustion over $Ru_xIr_{1-x}O_2$ supported on various carriers.

The pure carriers show practically no activity for propane combustion reaction in the considered temperature regions. In addition, Arrhenius plots are shown for the low conversion region. The variation in catalytic activity among the different compositions *x* is surprisingly small, in particular when compared with the catalytic methane combustion.[40] The effect of the carrier is mainly traced to the variation in dispersion of the active component $Ru_xIr_{1-x}O_2$.

Among the Ruxxx_Ce samples in Figure 5A, B the Ru100_Ce sample is the most active catalyst, while Ir100_Ce is the least active catalyst for the propane oxidation reaction. The activity (*STY* and *STYa* values, normalized to total mass of the catalysts and to the mass of the active component) decreases as Ru100_Ce > Ru075_Ce ≈ Ru050_Ce ≈ Ru025_Ce > Ir100_Ce. The

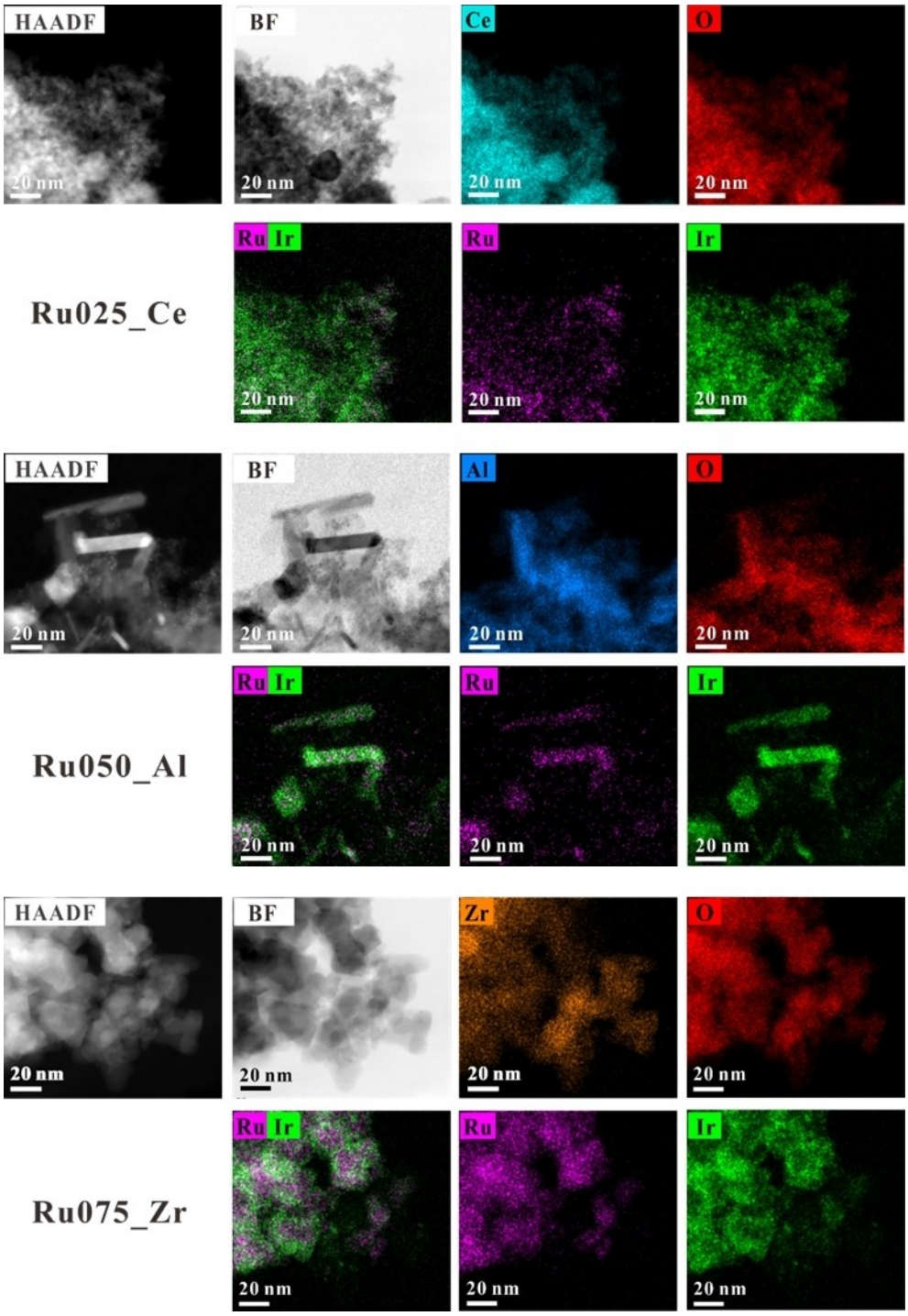

Figure 3. HAADF-STEM and bright field (BF) images are shown together with EDS mapping of Ru025_Ce (top), Ru050_Al (middle) and Ru075_Zr (bottom).

propane combustion activity is hardly affected by the actual composition of the Ru–Ir solid for *x* ranging from 0.25 to 0.75. However, already a concentration of 25% of Ru is sufficient to improve the activity by a factor of three compared to that of Ir100_Ce. As summarized in Table 3, the apparent activation energies E_a vary from 91 kJ/mol to 116 kJ/mol, revealing no substantial differences among the samples. The T_5 values denote the temperatures where the conversion is 5%. These temperatures are indicative of the required reaction temperature and are in the range 220±13 °C. The lowest T_5 is found with Ru100_Ce (207 °C) and the highest for Ir100_Ce with 233 °C.

Among the activity curves of Ruxxx_Al samples in Figures 5D, E, the Ru100_Al sample turns out to be most active, followed by Ru050_Al, Ru075_Al and Ru025-Al samples, while the Ir100_Al sample is again the least active catalyst for C_3H_8

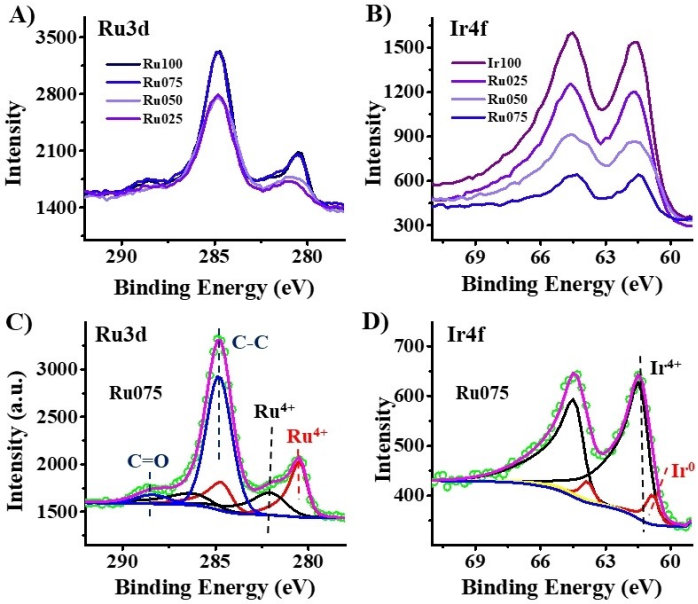

Figure 4. Ru 3d (A) and Ir 4f (B) XPS of the various $Ru_xIr_{1-x}O_2$-supported on ZrO_2 catalysts. The experiments (green open circle) are shown together with the decomposition into various species exemplified with the Ru075_Zr sample (C, D). The complete set of decompositions can be found in the supporting information.

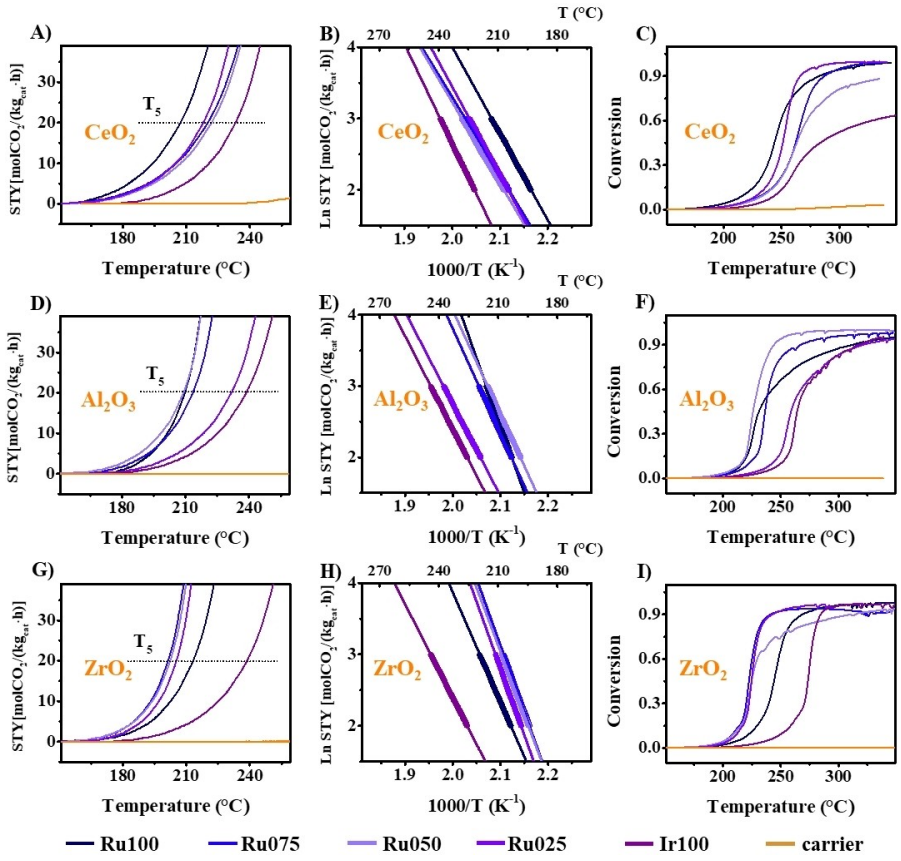

Figure 5. *STY* as a function of reaction temperature in the propane combustion over $Ru_xIr_{1-x}O_2$ that is supported on CeO_2 (A), γ-Al_2O_3 (D) and ZrO_2 (G). From these data Arrhenius plots are constructed (B, E, H). The circles indicate the experimental activity data where the conversion varies from 2% to 5%. Light off curves are shown in (C, F, I). C_3H_8 combustion reaction conditions: 1vol. % C_3H_8, 10 vol. % O_2, balanced by N_2; total volume flow: 115 mL/min (100 sccm), temperature ramp: 1 K/min.

Table 3. Activity data of $Ru_xIr_{1-x}O_2$ catalysts supported on various carriers (CeO_2, γ-Al_2O_3, ZrO_2) for propane combustion reactions.

carrier	Kinetic data	Ru100	Ru075	Ru050	Ru025	Ir100
CeO_2	*STY* (210 °C)	23	13	12	13	5
	STYa (210 °C)	575	278	224	215	74
	T_5 [°C]	207	220	222	218	233
	E_a [kJ/mol]	101	91	94	103	116
γ-Al_2O_3	*STY* (210 °C)	20	16	21	6.5	4
	STYa (210 °C)	153	105	120	33	18
	T_5 [°C]	210	213	209	231	239
	E_a [kJ/mol]	157	122	121	107	109
ZrO_2	*STY* (210 °C)	17	44	39	31	4
	STYa (210 °C)	320	708	547	386	45
	T_5 [°C]	213	201	202	205	239
	E_a [kJ/mol]	128	155	148	155	109

STY (210 °C): *STY* at a reaction temperature of 210 °C, given in mol(CO_2)/(h·kg(cat)). ***STYa*** (210 °C): *STYa* at a reaction temperature of 210 °C, given in mol(CO_2)/(h·kg(active component)) .T_5: temperature at which the conversion is 5 %.

oxidation reaction. The apparent activation energies E_a range from 107 kJ/mol to 157 kJ/mol (cf. Table 3). The T_5 values of the $Ru_xIr_{1-x}O_2$ supported on γ-Al_2O_3 for the propane oxidation are in the range of 220 ± 19 °C. The lowest T_5 temperature is found for Ru100_Al (210 °C) and the highest for Ir100_Al (239 °C).

The activity of the $Ru_xIr_{1-x}O_2$ supported on ZrO_2 is summarized in Figure 5G, H and Table 3. The ordering in activity is Ru100_Zr < Ru075_Zr ≈ Ru050_Zr > Ru025_Ce > Ir100_Ce. The most active catalyst is Ru075_Zr, indicating a synergy effect between Ru and Ir. The apparent activation energy reveals a narrow distribution around E_a of 153 ± 7 kJ/mol and the T_5 values of 203 °C ± 2 °C among the supported samples studied (except for Ru100_Zr and Ir100_Zr).

Altogether, RuO_2 supported on CeO_2 exhibits a slightly higher activity at low conversion. The most active catalyst for the propane combustion reaction at higher conversion is Ru075_Zr, while by far the lowest activity is encountered with Ir100, independent of the chosen carrier. For CeO_2 and ZrO_2 supported catalysts already 25 % Ru suffices to increase the activity by a factor of three and eight, respectively, with respect to pure Ir100.

In order to gain a deeper understanding of the stability of $Ru_xIr_{1-x}O_2$ on various carriers, long-term stability and water poisoning experiments for selected catalysts are conducted and compiled in Figure 6. We start the discussion with the long-term stability, i.e. the activity as a function of reaction time. ZrO_2-supported catalysts are surprisingly stable independent of the composition of the active component. Quite in contrast, the γ-Al_2O_3 supported catalysts indicates substantial loss in activity as a function of reaction time. For CeO_2-supported catalysts only pure RuO_2 is stable, the other active components containing Ir show slight deactivation of the catalyst with time on stream.

If 3 vol.% water is admitted to reaction feed, water poisoning is observed for all catalysts albeit with varying degree of deactivation. The deactivation due to water is reversible in all cases, meaning that when the water exposure is turned off the activity quickly recovers. A general trend is that the higher the Ir content of the active component the more severe is water poisoning.

The γ-Al_2O_3-supported catalysts reveal a severe deactivation due to water exposure: the pure IrO_2 component is highly susceptible to water poisoning, reducing the conversion from 80 % to below 40 %. For the CeO_2-supported catalysts, RuO_2 is quite stable even upon water exposure, while the Ir-containing catalysts exhibit significant deactivation. The ZrO_2-supported catalysts behave quite surprisingly: only little water poisoning is encountered even for pure supported IrO_2, while for pure RuO_2 water poisoning is practically not observed.

In summary, Ru100_Ce, Ru100_Zr, Ru075_Zr and Ir100_Zr are quite stable during the long-term stability test. For other samples, the activity slightly decreases with time on stream. IrO_2 is much more susceptible to water poisoning than RuO_2, independent of the chosen support. When water is added to the reaction mixture, the activity decreases to some extent, but after removing water from the reaction feed, the activity fully recovers. By far the ZrO_2 carrier shows highest water-poisoning resistance.

Discussion

Independent of the chosen carrier, supported mixed $Ru_xIr_{1-x}O_2$ particles are formed whose bulk (Vegard's law determined by XRD, Table 1 and elemental analysis, Table S4) and surface composition (XPS, Table 2) is close to the nominal compositions *x*. From XPS analysis (Table 2) the dispersion of the active component $Ru_xIr_{1-x}O_2$ is highest for CeO_2, followed by ZrO_2, while the lowest dispersion is encountered with γ-Al_2O_3. The high loading of 5 mol% of $Ru_xIr_{1-x}O_2$ enables the proper characterization of the catalysts by XRD, Raman spectroscopy, XPS, and STEM.

Pure IrO_2 is significantly less active than the other compositions independent of the carrier material. The highest activity is encountered with RuO_2-rich compositions. For low conversion Ru100_Ce is most active catalyst, while at high conversion Ru075_Zr reveals highest activity in the propane combustion. In particular, the Ru075_Zr is by a factor of two more active than Ru100_Zr, clearly pointing towards a synergy effect.

For the catalytic propane combustion IrO_2 is significantly less active than RuO_2, quite in contrast to the catalytic methane combustion where IrO_2 has shown to be much more active than RuO_2, both for powder and supported catalysts.[40] This difference in catalytic activity is correlated with the activation process of alkanes. In case of methane combustion, methane activation is rate limiting and IrO_2 is able to activate methane much more efficiently than RuO_2. In case of propane combustion, the actual propane activation step is not critical and can be accomplished by both RuO_2 and IrO_2. However, the subsequent oxidation steps of propane to form water and CO_2 are crucial, and here RuO_2 is obviously superior over IrO_2, so that overall RuO_2 is more active in the propane combustion than IrO_2. With temperature-programmed reaction experiments ruthenium was shown to be efficient in the activation of C–H and C–C bonds.[21] Once

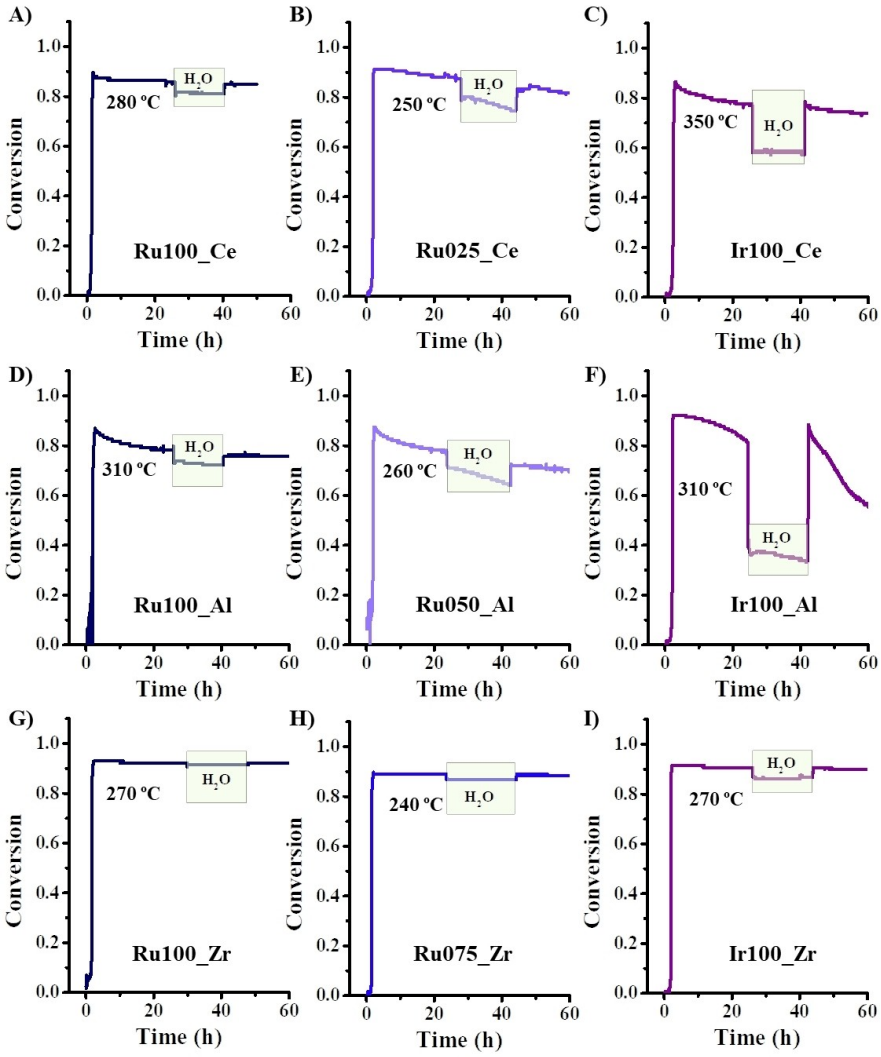

Figure 6. Long-term stability and water poisoning performance of A) Ru100_Ce, B) Ru025_Ce, C) Ir100_Ce. D) Ru100_Al, E) Ru050_Al, F) Ir100_Al, G) Ru100_Zr, H) Ru075_Zr, I) Ir100_Zr samples for the propane combustion reaction. The reaction temperature is varied among the different catalysts to keep the conversion around 90%.

the C–C bond of propane is broken, the methyl and ethyl groups are further oxidized similarly to the methyl group in the methane combustion.[17,54–58]

Besides catalytic activity, the stability of the catalyst is important in assessing the overall catalytic performance.[59–61] Long-term stability experiments (Figure 6) demonstrate a decline in activity as a function of time on stream, which depends critically on both, the carrier material and the composition of the active component. The γ-Al_2O_3 carrier reveals the most severe deactivation with reaction time. Nevertheless, XRD characterization (Table S1 and Figure S9), XPS experiments (Figure S10 and Tables S2, S3) and elemental analysis (Tables S4) after propane combustion reaction do not show substantial differences. The catalysts with the other two carriers are more stable in the propane combustion than γ-Al_2O_3, although ZrO_2-supported catalysts seem to be slightly more stable than the CeO_2-supported ones, in particular when the active component contains higher concentration of Ir.

In case of methane combustion, it is well documented that water acts as catalyst poison.[41] For the catalytic propane combustion, Figure 6 reveals water poisoning that turns out to be reversible. As soon as water exposure is turned off, the activity recovers for all studied catalysts. This observation is traced to a simple blocking of active sites of the active component due to reversible water adsorption. As summarized in Figure 6, water poisoning depends critically on the composition x of $Ru_xIr_{1-x}O_2$. Pure RuO_2 is much less prone to water poisoning than pure IrO_2, and the higher the Ir concentration the more severe water poisoning becomes. This behavior can be traced to the different interaction strength of water with RuO_2 and IrO_2. In previous surface science experiments, it has been shown that water is less strongly adsorbed on RuO_2(110)[62–63] than on IrO_2(110).[64] Water desorbs from RuO_2(110) and IrO_2(110) at around 170 °C[62] and 270–320 °C,[64] respectively. This means that water is capable to block active sites under reaction conditions, and this blocking is less severe

for RuO_2 than for IrO_2, fully consistent with the experiments in Figure 6. Secondly, water poisoning is reversible, since at temperatures of 250–300 °C water can efficiently desorb from the surface of the active component, as soon as water exposure is turned off.

Quite surprisingly, water poisoning of the supported catalysts depends also on the carrier material (cf. Figure 6). The catalysts supported on γ-Al_2O_3 turned out to be more susceptible to water poisoning than catalysts on the other carriers, while $Ru_xIr_{1-x}O_2$ on ZrO_2 is slightly more resistant against water poisoning than on CeO_2. The degree of water poisoning follows roughly the long-term stability without water in the reaction feed. In case the catalysts reveal a substantial decline in activity with time on stream, these catalysts undergo also an enhanced degree of water poisoning. The dependence of water poisoning with the carrier is, however, not expected when only the active component is assumed to determine the catalytic turnover. Therefore, the interaction of water with the carrier needs to be considered in a mechanistic discussion of propane combustion. Maybe the triple phase boundaries of the active component with the carrier contributes to the catalytic conversion of propane, or the accommodated water on the carrier can affect the reaction steps in the propane combustion over the active component.

Conclusions

Catalysts of 5 mol% $Ru_xIr_{1-x}O_2$ ($x = 0$, 0.25, 0.5, 0.75, 1.0) supported on CeO_2, γ-Al_2O_3 or ZrO_2 are successfully prepared and tested in the catalytic propane combustion in terms of activity and stability. The active component $Ru_xIr_{1-x}O_2$ constitutes a mixed oxide, i.e. a solid solution, with bulk and surface compositions that are close to the nominal compositions *x*. The high loading of 5 mol% of the active component was chosen to enable detailed characterization with XRD and Raman spectroscopy.

For all carriers pure IrO_2 reveals a significantly lower activity, while the highest activity in propane combustion is encountered with RuO_2-rich active components. This emphasizes the decisive role of RuO_2 governing the activity in propane combustion. For low conversion, Ru100_Ce turns out to be the most active catalyst, while at higher conversions Ru075_Zr is found to be the most active one, pointing towards a slight synergy effect.

Long-term stability is highest for ZrO_2-supported catalysts, while those supported on γ-Al_2O_3 are practically unstable. Also the resistance against water poisoning is highest for the ZrO_2-supported catalysts. The higher the Ir concentration of the active component $Ru_xIr_{1-x}O_2$ the more prone is the catalyst to water poisoning. Therefore, thermal stability by mixing with iridium is improved only at the expense of higher degree of reversible water poisoning. Water poisoning is shown to be reversible in all cases, consistent with blocking of catalytically active sites by water adsorption.

The presented activity and stability experiments for propane combustion may provide a promising guidance for developing active and durable RuO_2-based supported catalysts for the removal of short-chain volatile organic compound. A promising carrier material is ZrO_2 that makes $Ru_xIr_{1-x}O_2$ particularly resistant against water poisoning.

Experimental Details

Preparation of catalysts

Supported ruthenium-iridium mixed oxide samples are prepared by a modified sol-gel method[40,65] with the mole percentage of (Ru + Ir)/carrier being 5 mol%. Such a (high) content of 5 mol% of the active component is chosen in order to be able to characterize the various catalysts properly, in particular with X-ray diffraction (XRD). The composition of the active component varies from pure IrO_2 to RuO_2 via three particular mixed oxides $Ru_{0.25}Ir_{0.75}O_2$, $Ru_{0.50}Ir_{0.50}O_2$, and $Ru_{0.75}Ir_{0.25}O_2$ which are supported on commercial CeO_2 (Sigma-Aldrich), ZrO_2 (Saint-Gobain NorPro) and γ-Al_2O_3 (Ionic Liquids Technologies). Samples of ruthenium-iridium mixed oxides supported on CeO_2 are denoted as Ruxxx_Ce (xxx: mol% of Ru) or Irxxx_Ce (xxx: mol% Ir); analogous abbreviations are employed for the other carriers as Ruxxx_Al and Ruxxx_Zr. We exemplify the synthesis with $Ru_{0.50}Ir_{0.50}O_2$ supported on CeO_2 sample (denoted as Ru050_Ce): first 0.15 mmol of $RuCl_3 \cdot 3.5\ H_2O$ (Acros Organics) and 0.15 mmol of $IrCl_4 \cdot H_2O$ (Fluorochem) are dissolved in deionized water, 5.81 mmol (1 g) CeO_2 are added to the solution, and the suspension is stirred for 10 min. Subsequently, 15 mmol of anhydrous citric acid are added to the mixture and continuously stirred for half an hour. Mild heating to 60 °C accomplishes the complete complexation of the metal cations. Subsequently 45 mmol ethylene glycol are added and the mixture is heated to 100 °C. As soon as most of the solvent is evaporated, the resulting black/gray resin is collected and annealed at 450 °C for 12 h with a heating rate of 1 K/min. The obtained Ru050_Ce sample is ground for the characterization and catalytic experiments. Other samples were prepared accordingly by adjusting the ruthenium and iridium concentration and the carrier. With XPS we carefully checked that no contamination of Cl^- of the catalyst's samples takes place.

Characterization of catalysts

Powder X-ray diffraction (XRD) patterns are recorded with a Panalytical X'Pert PRO diffractometer by using a Cu K_α source (40 kV, 40 mA). The Raman spectra are collected on a Senterra spectrometer of Bruker Optics at ambient condition and processed with OPUS 7.5 software. The wavelength of the excitation laser was 532 nm. All samples are measured with a spectral resolution of 3 ~ 5 cm^{-1}, 20 co-addition, and 10 seconds integration time.

The samples are pre-treated at 120 °C for 12 h in vacuum before performing Kr physisorption experiments with an Autosorb 6 instrument (Quantachrome). The specific surface

area is quantified by applying the BET (Brunauer-Emmett-Teller) method. The BET surface areas of the carriers used in this study are 30 m^2/g (CeO_2), 100 m^2/g (γ-Al_2O_3) and 35 m^2/g (ZrO_2).

Scanning transmission electron microscopy (STEM) characterization is carried out with a Thermo Fisher Talos F200X transmission electron microscope that is equipped with a field-emission electron gun (FEG) operated at 200 kV. For element mapping both high angle annular dark field (HAADF)-STEM and energy dispersive X-ray spectroscopy (EDS) data are taken from the same region of the sample. The TEM samples are prepared by dispersing the catalyst powder in ethanol first and subsequently bringing a droplet of the solution onto a copper grid and evaporating the solvent.

With X-ray photoelectron spectroscopy (XPS: PHI VersaProbe II) the composition and chemical state of the samples in the near surface region can be determined. The photon energy is 1486.6 eV (monochromatized Al-K_α line). CasaXPS Version 2.3.17 is applied to analyze the XP spectra of Ru 3d, Ir 4f, Ce 3d, Zr 3d and Al 2p; the binding energy is calibrated to C 1s at 284.8 eV. The actual bulk concentrations of iridium and ruthenium in the various samples before and after propane combustion are quantified by ICP-AES (cf. Table S4), using a a Zeiss Merlin scanning electron microscopy and an acceleration voltage of 2 kV and a probe current of 100 pA.

Catalytic tests

Catalytic tests are conducted in a home-built flow reactor apparatus.[38] 20 mg of catalyst (pellet size was about 100 μm) are physically mixed with 40 mg of quartz sand and packed in a quartz tube with an inner diameter of 6 mm and a height of 1.5 mm. The gas mixture consisting of 89% N_2 (carrier gas), 10% O_2, and 1% C_3H_8 is fed into the reactor. The catalytic tests are conducted at high volumetric flow rates ($\dot{V}_0$) of 115 mL/min (100 sccm) that corresponds to a gas hourly space velocity of about 345,000 $ml\,g^{-1}\,h^{-1}$ if normalized to the average mass of catalyst. This allows for kinetic measurements within micro-kinetic region. A cycle consists of temperature ramp starting from room temperature to 370 °C with a rate of 1 K/min. For each sample several cycles are measured. The first cycle serves as a pretreatment, and the second cycle is chosen for the catalytic activity data.

The volumetric CO, CO_2, and C_3H_8 concentration are detected by a nondispersive infrared (NDIR)-sensor. A mass flow meter (measures $\dot{V}_1$) is required to quantify the space time yield (*STY*) after passing the reactor and analyzer. The *STY* is defined as the molar amount of CO_2 per time and mass catalyst. In addition, *STYa* values (where the *STY* is normalized to the mass of active component $Ru_xIr_{1-x}O_2$) are given to better compare the activity between various samples. Before the reaction, the total mass flow is ~115 ml/min, and when propane was fully consumed, the total mass flow was ~110.5 ml/min. According to the reaction equation 1 $C_3H_8 + 5\ O_2 = 3\ CO_2 + 4\ H_2O$, the missing flow of ~4.5 ml/min is due to the elimination of H_2O before the mixed gas goes into the analyzer. As expected, the concentration of CO_2 is found to be three times that of the propane concentration at the inlet. Combined with the missing gas of ~4.5 ml/min this provides clear evidence for the total oxidation of propane during the reaction. Since the total mass flow only changed from 115 ml/min to 110.5 ml/min, we calculated the conversion by $X = 1\text{-}c\ (C_3H_8)/c_0\ (C_3H_8)$, with c ($C_3H_8$) and c_0 (C_3H_8) being the volumetric concentration of propane leaving the reactor and the maximum volumetric concentration of propane in the gas mixture, respectively. The conversion curves that are calculated by the concentration of CO_2 and C_3H_8 are virtually identical, indicating no further by-product is formed. In particular, our detector does not record any CO concentration during the whole temperature scan of the catalytic test, which means the selectivity towards CO_2 is approaching 100%. When calculating the *STY*, we assumed the change of total mass flow (changed from 115 to 110.5 ml/min) is linearly related to conversion rate (0 to 100%).

Acknowledgements

This work was supported by National Natural Science Foundation of China (21922602, 22076047, U21A20326), the Shanghai Science and Technology Innovation Action Plan (20dz1204200) and Fundamental Research Funds for the Central Universities. Zheng Wang gratefully acknowledge the China Scholarship Council for the Joint-Ph.D. program between the China Scholarship Council and the Institute of Physical Chemistry of the Justus-Liebig-University Giessen. We acknowledge support from the Center for Materials Research at the JLU. Open Access funding enabled and organized by Projekt DEAL.

Conflict of Interest

The authors declare no conflict of interest.

Data Availability Statement

The data that support the findings of this study are available from the corresponding author upon reasonable request.

Keywords: total oxidation · propane · $Ru_xIr_{1-x}O_2$ · water poisoning

[1] H. Hao, Z. W. Liu, F. Q. Zhao, W. Q. Li, *Renewable Sustainable Energy Rev.* **2016**, *62*, 521–533.
[2] S. Colussi, A. Gayen, J. Llorca, C. Leitenburg, G. Dolcetti, A. Trovarelli, *Ind. Eng. Chem. Res.* **2012**, *51*, 7510–7517
[3] G. Veser, M. Ziauddin, L. D. Schmidt, *Catal. Today* **1999**, *47*, 219–228.
[4] R. Burch, P. K. Loader, F. J. Urbano, *Catal. Today* **1996**, *27*, 243–248.
[5] Q. G. Dai, Q. Zhu, Y. Lou, X. Y. Wang, *J. Catal.* **2018**, *357*, 29–40.
[6] X. W. Yang, Q. Li, E. Lu, Z. Q. Wang, X. Q. Gong, Z. Y. Yu, Y. Guo, L. Wang, Y. L. Guo, W. C. Zhan, J. S. Zhang, S. Dai, *Nat. Commun.* **2019**, *10*, 1611.
[7] H. Hao, B. F. Jin, W. Liu, X. D. Wu, F. F. Yin, S. Liu, *ACS Catal.* **2020**, *10*, 13543–13548.
[8] B. H. Cen, C. Tang, J. Q. Lu, J. Chen, M. F. Luo, *Chin. J. Catal.* **2021**, *42*, 2287–2295.

[9] H. Jeong, G. Lee, B. S. Kim, J. Bae, J. W. Han, H. Lee, *J. Am. Chem. Soc.* **2018**, *140*, 9558–9565.
[10] Y. F. Jian, Z. Y. Jiang, C. He, M. J. Tian, W. Y. Song, G. Q. Gao, S. N. Chai, *Catal. Sci. Technol.* **2021**, *11*, 1089–1097.
[11] E. V. Kovalyov, E. M. Sadovskaya, B. S. Bal′zhinimaev, *Chem. Eng. J.* **2018**, *349*, 547–553.
[12] C. P. O'Brien, I. C. Lee, *J. Catal.* **2017**, *347*, 1–8.
[13] W. M. Liao, X. X. Fang, B. H. Cen, J. Chen, Y. R. Liu, M. F. Luo, J. Q. Lu, *Appl. Catal. B* **2020**, *272*, 118858.
[14] Q. Q. Wu, J. R. Yan, M. X. Jiang, Q. G. Dai, J. Y. Wu, Q. P. Ke, X. Y. Wang, W. C. Zhan, *Appl. Catal. B* **2021**, *286*, 119949.
[15] P. P. Zhao, J. Chen, H. B. Yu, B. H. Cen, W. Y. Wang, M. F. Luo, J. Q. Lu, *J. Catal.* **2020**, *391*, 80–90.
[16] T. Cai, W. Deng, P. Xu, J. Yuan, Z. Liu, K. F. Zhao, Q. Tong, D. N. He, *Chem. Eng. J.* **2020**, *395*, 125071.
[17] L. Ma, Y. Geng, X. Y. Chen, N. Q. Yan, J. H. Li, J. W. Schwank, *Chem. Eng. J.* **2020**, *402*, 125911.
[18] Y. X. Wang, D. Y. Li, K. Z. Li, R. Farrauto, *Appl. Catal. B* **2020**, *267*, 118363.
[19] W. D. Zhang, K. Lassen, C. Descorme, J. L. Valverde, A. Giroir-Fendler, *Appl. Catal. B* **2011**, *282*, 119566.
[20] Z. Hu, S. Qiu, Y. You, Y. Guo, Y. L. Guo, L. Wang, W. C. Zhan, Guanzhong Lu, *Appl. Catal. B* **2018**, *225*, 110–120.
[21] C. G. Freyschlag, R. J. Madix, *Mat. Tod.* **2011**, *14*, 134–142.
[22] J. Okal, M. Zawadzki, *Catal. Lett.* **2009**, *132*, 225–234.
[23] J. Okal, M. Zawadzki, L. Krajczyk, *Catal. Today* **2011**, *176*, 173–176.
[24] J. Okal, M. Zawadzki, P. Kraszkiewicz, K. Adamska, *Appl. Catal. A* **2017**, *549*, 161–169.
[25] Z. Hu, Z. Wang, Y. Guo, L. Wang, Y. L. Guo, J. S. Zhang, W. C. Zhan, *Environ. Sci. Technol.* **2018**, *52*, 9531–9541.
[26] Z. Wang, Z. P. Huang, J. T. Brosnahan, S. Zhang, Y. L. Guo, Y. Guo, L. Wang, Y. S. Wang, W. C. Zhan, *Environ. Sci. Technol.* **2019**, *53*, 5349–5358.
[27] Z. Wang, O. Khalid, W. Wang, Y. Wang, T. Weber, A. S. Luciano, W. C. Zhan, B. Smarsly, H. Over, *Catal. Sci. Technol.* **2021**, *11*, 6839–6853.
[28] Z. Zhu, G. Lu, Y. Guo, Y. Guo, Z. Zhang, Y. Wang, X.-Q. Gong, *ChemCatChem* **2013**, 5, 2495–2503.
[29] K. A. Ledwa, M. Pawlyta, L. Kępiński, *Appl. Catal. B* **2018**, *230*, 135–144.
[30] K. A. Ledwa, L. Kępiński, M. Ptak, R. Szukiewicz, *Appl. Catal. B* **2020**, *274*, 119090.
[31] K. Adamska, J. Okal, W. Tylus, *Appl. Catal. B* **2019**, *246*, 180–194.
[32] K. Baranowska, J. Okal, *Appl. Catal. A* **2015**, *499*, 158–167.
[33] K. Baranowska, J. Okal, *Catal. Lett.* **2016**, *146*, 72-81.
[34] K. Baranowska, J. Okal, *Top. Catal.* **2017**, *60*, 266-271.
[35] W. M. Liu, S. Y. Yang, Q. L. Zhang, T. Y. He, Y. W. Luo, J. X. Tao, *Appl. Catal. B* **2021**, *292*, 120171.
[36] J. Chen, X. L. Lv, W. J. Xu, X. L. Li, J. Chen, *Appl. Catal. B* **2021**, *290*, 119989.
[37] R. Kötz, S. Stucki, *Acta* **1986**, *31*, 1311–1316.
[38] F. I. Mattos-Costa, P. De Lima-Neto, S. A. S. Machadao, L. A. Avaca, *Acta* **1998**, *44*, 1515–1523.
[39] O. Khalid, T. Weber, G. Drazic, I. Djerdj, H. Over, *J. Phys. Chem. C* **2020**, *124*, 18670–18683.
[40] O. Khalid, A. Spriewald-Luciano, D. Drazic, H. Over, *ChemCatChem* **2021**, *13*, 1–13.
[41] N. M. Kinnunen, J. T. Hirvi, K. Kallinen, T. Maunula, M. Keenan, M. Suvanto, *Appl. Catal. B* **2017**, *207*, 114–119.
[42] Q. G. Dai, J. Y. Wu, W. Deng, J. S. Hu, Q. Q. Wu, L. M. Guo, W. Sun, W. C. Zhan, X. Y. Wang, *Appl. Catal. B* **2019**, *249*, 9–18.
[43] C. F. Cullis, T. G. Nevell, D. L. Trimm, *J. Chem. Soc. Faraday Trans. 1* **1972**, *68*, 1406–1412.
[44] R. Butch, F. J. Urbano, P. K. Loader, *Appl. Catal. A* **1995**, *123*, 173–184.
[45] P. Gelin, M. Priomet, *Appl. Catal. B* **2002**, *39*, 1–37.
[46] A. Toso, S. Colussi, S. Padigapaty, C. de Leitenburg, A. Trovarelli, *Appl. Catal. B* **2018**, *230*, 237–245.
[47] P. Marecot, A. Fakche, B. Kellau, G. Mabilon, M. Prigent, J. Barbier, *Appl. Catal. B* **1994**, *4*, 283–294.
[48] W. X. Tang, W. Xiao, S. B. Wang, Z. Ren, J. Ding, P. X. Gao, *Appl. Catal. B* **2018**, *226*, 585–595.
[49] Y. B. Zheng, Y. Y. Chen, E. H. Wu, X. P. Liu, B. Q. Huang, H. Xue, C. L. Cao, Y. J. Luo, Q. R. Qian, Q. H. Chen, *Chem. Eur. J.* **2021**, *27*, 4738–4745.
[50] X. S. Feng, F. Q. Luo, Y. Y. Chen, D. F. Lin, Y. J. Luo, L. R. Xiao, X. P. Liu, X. L. Sun, Q. R. Qian, Q. H. Chen, *J. Hazard. Mater.* **2021**, *406*, 124695.
[51] K. Murata, J. Ohyama, Y. Yamamoto, S. Arai, A. Satsuma, *ACS Catal.* **2020**, 10, 8149–8156.
[52] W. X. Huang, X. R. Zhang, A. C. Yang, E. D. Goodman, K. C. Kao, M. Cargnello, *ACS Catal.* **2020**, *10*, 8157–8167.
[53] S. Wendt, A. P. Seitsonen, Y. D. Kim, M. Knapp, H. Idriss, H. Over, *Surf. Sci.* **2002**, *505*, 137–1152.
[54] T. F. Garetto, E. Rincón, C. R. Apestegua, *Appl. Catal. B* **2004**, *48*, 167–174.
[55] E. K. Novakova, J. C. V'edrine, E. G. Derouane, *J. Catal.* **2002**, *211*, 235–243.
[56] R. D. Wilk, N. P. Cernansky, R. S. Cohen, *Combust. Sci. Technol.* **1986**, *49*, 41–78.
[57] B. Wang, X. D. Wu, R. Ran, Z. C. Si, D. Weng, *J. Mol. Catal. A* **2012**, *356*, 100–105.
[58] A. Hinz, M. Skoglundh, E. Fridell, A. Andersson, *J. Catal.* **2001**, *201*, 247–257.
[59] M. D. Argyle, C. H. Bartholomew, *Catalysts* **2015**, *5*, 145–269.
[60] S. L. Scott, *ACS Catal.* **2018**, *8*, 8597–8599.
[61] F. Hess, B. M. Smarsly, H. Over, *Acc. Chem. Res.* **2020**, *5*, 380–389.
[62] A. Lobo, H. Conrad, *Surf. Sci.* **2003**, *523*, 279–286.
[63] M. Knapp, D. Crihan, A. P. Seitsonen, E. Lundgren, A. Resta, J. N. Andersen, H. Over, *J. Phys. Chem. C* **2007**, *111*, 5363–5373.
[64] T. Li, M. Kim, Z. Liang, A. Asthagiri, J. F. Weaver, *Top. Catal.* **2018**, *61*, 397–411.
[65] M. P. Pechini, *US Patent* **1967**, 3.330.697.

Manuscript received: January 31, 2022
Revised manuscript received: April 1, 2022
Accepted manuscript online: April 8, 2022
Version of record online: April 27, 2022